

Estimating energy input rate from vertical profiles of energy dissipation rate

Nozomi Sugiura^{1,*}, Shinya Kouketsu¹, Shuhei Masuda¹, Satoshi Osafune¹, and Ichiro Yasuda²

¹Research and Development Center for Global Change, JAMSTEC, Yokosuka, Japan

²Atmosphere and Ocean Research Institute, University of Tokyo, Chiba, Japan

*nsugiura@jamstec.go.jp

ABSTRACT

The energy dissipation rate is an important characteristic of turbulence; however, its magnitude in observational profiles can be misidentified owing to its erratic evolution. By analyzing observed data from oceanic turbulence, we show that the vertical sequences of depth-averaged energy dissipation rates have a scaling property. We propose a method to estimate the energy input rate by utilizing this property. It is found that for scaling in the observed profiles, our data have a statistical property consistent with the universal multifractal model, which comprises α -stable generators with parameters $\alpha = 1.74$ and $C_1 = 0.393$. This determines the averaging rule of the energy dissipation rates in the logarithmic space. Meanwhile, the energy input rate and its uncertainty given observation can be estimated by inverting the probability distribution obtained by Monte Carlo simulations of the cascade model, through adding additional information to the arithmetic average over the vertical data sequence.

Introduction

The importance of determining the energy dissipation rate to study ocean general circulation has been highlighted in numerous studies^{1,2}. Hence, a large number of observational studies have been conducted to obtain the vertical profiles of the energy dissipation rate using ocean microstructure profilers^{3,4}. In addition, to understand the statistics of the erratic evolution of observational profiles, studies have been conducted from the viewpoint of statistical fluid mechanics, as summarized below.

In fully developed turbulence, there exists an inertial subrange where the advective term is dominant over the molecular viscosity term in the Navier–Stokes equation⁵. In the inertial subrange, there is a cascade of energy from large to small, as intuitively stated by Richardson⁶. As the first quantitative theory on the energy cascade, Kolmogorov⁷ established a relationship wherein velocity fluctuations are locally isotropic and are determined by the homogeneous energy dissipation rate,

$$\langle |v(x+\ell) - v(x)| \rangle \approx \varepsilon^{1/3} \ell^{1/3}, \quad (1)$$

where $\langle \cdot \rangle$ denotes the ensemble average. Subsequently, it was criticized that the energy dissipation rate is not homogeneous but shows significant random fluctuations⁸. A refined theory was proposed to address this issue⁹. The theory stated that i) $\log \varepsilon_r$, which is the logarithm of the spatially averaged energy dissipation rate over scale r , obeys a Gaussian distribution, and ii) its variance obeys $\sigma_{\log \varepsilon_r}^2 = A + \mu \log(L/r)$ (L : the outer scale).

Additionally, several experimental studies^{10,11} showed that small-scale dissipation is a random field that has a spatial structure with power-law correlations,

$$\langle \varepsilon(x)\varepsilon(x+\ell) \rangle \propto \ell^{-\mu}. \quad (2)$$

Then, Yaglom¹² formulated a quantitative model, which was consistent with the scaling log-normality and the power-law correlations, as a multiplicative cascade, where ε_r was expressed with a binary tree composed of i.i.d random variables, $W_{i,k}$ ($\sim W$),

$$\forall 1 \leq j \leq 2^n, \quad \varepsilon_r(x_j) = \prod_{i=1}^n W_{i,[(j-1)/2^{n-i}]+1}, \quad (3)$$

where $[\cdot]$ is the Gauss symbol. If the random variables are set to have the moment exponent, $K(q) = \log_2 \langle W^q \rangle = (\mu/2)(q^2 - q)$, then the energy conservation and the log-normality at each scale in⁹ are reproduced. Moreover, correlation (2) is reproduced because we have $\langle \varepsilon(x)\varepsilon(x+\ell) \rangle = \langle W^2 \rangle^{n-m} \langle W \rangle^{2m} \propto \ell^{-K(2)}$, where $L = 2^n r$, $\ell = 2^m r$ for small r ^{12,13}.

There have been several alternative multiplicative cascade models with different generators, including the β -model¹⁴, random β -model¹⁵, α -model¹⁶, p -model¹⁷, log-stable model¹⁸, and log-Poisson model¹⁹. An important observation regarding Yaglom's cascade is that the property required for the law of random variable W can be abstracted such that the product of several random variables still obeys the same class of distribution, $\prod_{i=1}^n W_i \sim a_n W^{b_n}$, with $a_n, b_n > 0$ ²⁰. Consistent with this condition, the universal multifractal model¹⁸ employs a stable Lévy generator, Γ , that is maximally left skewed, and $W = e^\Gamma$ is set. This results in a simple and nonanalytic form of the moment exponent, $K(q) = (C_1/(\alpha - 1))(q^\alpha - q)$. The universal multifractal model is the most promising model. It can be used to model the variability in several phenomena including turbulence, other geophysical phenomena, and several fractal-like appearances in natural objects and even man-made objects.

Based on this theory, we reconsider one of the basic questions in the observational study of ocean turbulence: how can one estimate energy intensity, or the energy input rate, from the vertical profile data of the energy dissipation rate, which has been commonly equated with the arithmetic mean over the profile. Our question pertains to whether one can obtain information regarding energy intensity beyond the arithmetic average. The answer is yes because we can construct a model for the turbulent cascade process and solve the inversion problem to obtain the energy input rate under an observational constraint. In this study, we first show that the observed profiles of the depth-averaged energy dissipation rate, ε_r , have a scaling property that is consistent with the universal multifractal model. Then, we construct a multiplicative cascade simulation model that describes the statistics in observational data. We propose a method to explain certain statistics of the observed profiles based on a simulation model and develop an inversion method to estimate the energy input rate. This result should provide a systematic method of gaining further quantitative information from profile data.

The remainder of this paper is organized as follows: Section 2 describes the turbulence observation data. Section 3 describes the scaling analysis of the moments to derive the moment scaling exponent within the universal multifractal framework. Section 4 discusses the methods for estimating several quantities from observational data based on simulation and inference using the cascade model. Finally, section 5 concludes the paper.

1 Observational data

In this section, we describe the turbulence observational data employed in this study. The turbulence observational data were retrieved from the Pacific ocean (Fig. 1)²¹, and they comprise approximately 400 profiles, each of which typically extends over a depth of 2000 to 6000 m below the sea surface, with observational points every 5 to 10 m.

The turbulent energy dissipation rates, ε , were estimated as follows: Microscale temperature fields were observed using the fast-response Fasttip Probe model 07 (FP07) thermistors attached to frames for measuring conductivity, temperature, and depth (CTD) as common oceanographic observational platforms. ε was derived by detecting the Batchelor wavenumber²² and fitting²³ a theoretical spectrum²⁴ to the observed temperature vertical gradient spectra after correcting the spectra with a double-pole function with a time constant of 3ms²⁵. Each data point was evaluated for a depth interval of approximately 10m with half overlap to yield 5dbar interval data. Herein, we included all data without any quality screening to consider the extreme values, which are important for investigating intermittency.

We estimated the turbulent energy dissipation rate from temperature measurement in each observational bin with a width of $r_0 \simeq 10\text{m}$ by utilizing a fitting method based on analytical spectral closure (see Appendix A for the estimation principle). We restricted our investigation to the intermittency occurring at larger scales, $r > r_0$.

Let r_0 be the bin width, \vec{x}_j the horizontal coordinate of the j -th profile, and z_k the vertical coordinate of the k -th point in the j -th profile. These positive-valued data have the following characteristics:

1. Each profile defines an ordered set,

$$\left\{ \varepsilon_{r_0}(\vec{x}_j, z_{k_j}) \middle| k_j = 1, 2, \dots, K_j \right\},$$

which exhibits an extremely erratic evolution that impedes the recognition of a continuous curve along the depth direction (Fig. 2(a)).

2. After taking the logarithm of the values, the sequences appear to be more continuous (Fig. 2(b)).
3. If we normalize each value with the arithmetic mean along the profile it belongs to, the histogram of the logarithmic values,

$$\left\{ \log \left(\frac{\varepsilon_{r_0}(\vec{x}_j, z_{k_j})}{K_j^{-1} \sum_{k_j} \varepsilon_{r_0}(\vec{x}_j, z_{k_j})} \right) \middle| j = 1, 2, \dots, J; k_j = 1, 2, \dots, K_j \right\},$$

appears as an asymmetric distribution (cyan in Fig. 6), which is discussed below.

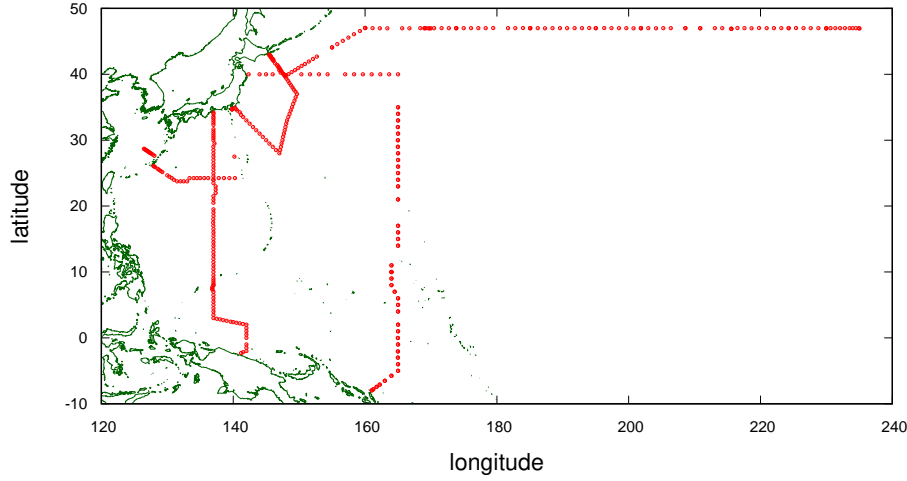


Figure 1. Horizontal locations of the observed profiles (red) and land–sea boundaries (green). The units of longitude and latitude are °E and °N, respectively.

2 Multifractal analysis

We perform the scaling analysis of the moments to derive the moment scaling exponent within the universal multifractal framework. Although the analysis could be extended to multidimensional objects²⁶, the limited number of samples (400 profiles) prevents us from a meaningful treatment in a multidimensional framework. Therefore, we treat each profile as an independent sample, and analyze the statistical structure of the 1-dimensional object. One exception applies for repeated observations at the same horizontal location (see sec. 3.2.4).

2.1 Universal multifractal model

The basic formulation of the universal multifractal model is as follows^{26,27}: Suppose we have a multifractal field, ε_λ , at resolution λ ($= L/r$), where r is the observational scale and L is the outer scale. The field is normalized by the mean, $\langle \varepsilon_\lambda \rangle = \langle \varepsilon \rangle$, which is conserved at all scales.

The probability of exceeding a scale-dependent threshold, λ^γ , varies according to singularity γ as

$$Pr(\varepsilon_\lambda \geq \lambda^\gamma) \approx \lambda^{-c(\gamma)}, \quad (4)$$

where $c(\gamma)$ is the codimension function and \approx represents the equality up to the multiplication of a slowly varying function of γ . Thus, the multifractal model is characterized by the property that the codimension varies with the singularity. This relation is equivalently represented as the scaling of the statistical moment of any order, q ,

$$\langle (\varepsilon_\lambda)^q \rangle = \lambda^{K(q)}, \quad (5)$$

where $K(q)$ is the moment scaling function. The two functions, $K(q)$ and $c(\gamma)$, are actually compatible by the Legendre transformation because the moment generation function can be written in terms of the occurrence probability of singular events using the saddle-point approximation, $\langle (\varepsilon_\lambda)^q \rangle = \int \lambda^{q\gamma} dp(\gamma) \approx \lambda^{\max_\gamma \{q\gamma - c(\gamma)\}}$ ²⁸. Functions $K(q)$ and $c(\gamma)$ determine the variability of multifractal field ε_λ across the scales, λ .

Owing to a generalization of the central limit theorem, many multiplicative processes composed of different generators converge to a universal multifractal^{18,29}, whose moment exponent has the following form:

$$K(q) = \frac{C_1}{\alpha - 1} (q^\alpha - q), \quad (6)$$

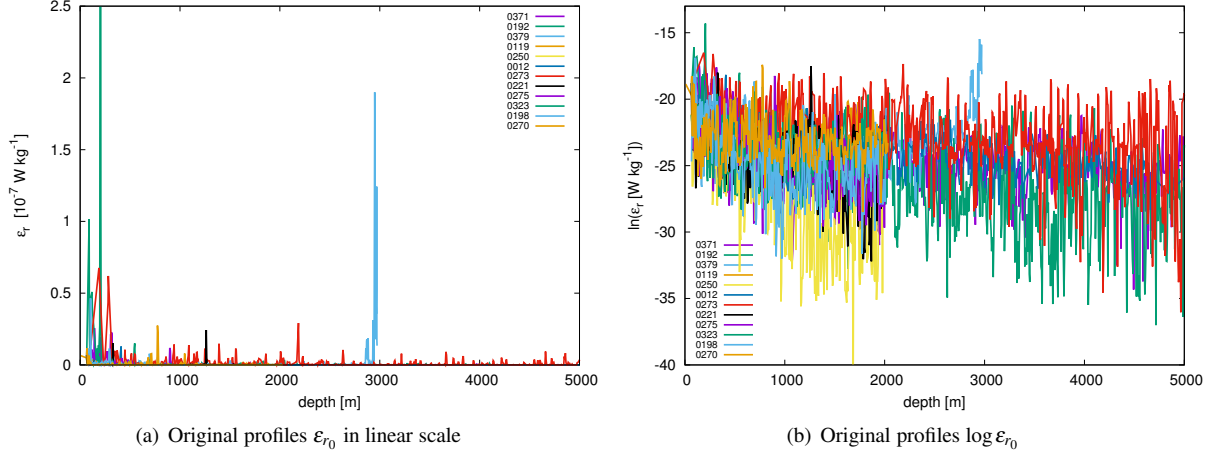


Figure 2. Appearances of observed profiles.

where $0 \leq \alpha \leq 2$ is the multifractal index and C_1 is the codimension of the mean. This also satisfies probability normalization, $K(0) = 0$, and energy conservation, $K(1) = 1$. The Legendre transformation of this gives $c(\gamma)$ in the following form:

$$c(\gamma) = C_1 \left(\frac{\gamma}{C_1 \alpha'} + \frac{1}{\alpha} \right)^{\alpha'}, \quad (7)$$

where $1/\alpha + 1/\alpha' = 1$.

2.2 Analysis of observational data

Suppose we have the observational data of the energy dissipation rate, $\varepsilon_r(\vec{x})$, in bin width r_0 at horizontal position \vec{x} and their spatial average $\varepsilon_r(\vec{x})$ in width r . In terms of these data, Eq. (5) reads

$$\frac{\langle (\varepsilon_r(\vec{x}))^q \rangle}{\langle \varepsilon(\vec{x}) \rangle^q} = \left(\frac{L}{r} \right)^{K(q)}, \quad (8)$$

$$\frac{\langle (\varepsilon_{r_0}(\vec{x}))^q \rangle}{\langle \varepsilon(\vec{x}) \rangle^q} = \left(\frac{L}{r_0} \right)^{K(q)}. \quad (9)$$

By dividing Eq. (9) by Eq. (8), we obtain

$$\frac{\langle (\varepsilon_{r_0}(\vec{x}))^q \rangle}{\langle (\varepsilon_r(\vec{x}))^q \rangle} = \left(\frac{r}{r_0} \right)^{K(q)}, \quad (10)$$

for arbitrary horizontal position \vec{x} .

Based on Eq. (10), we perform a scaling analysis of observational data with respect to various moment exponents, q , by estimating the slope of the approximation straight line for the observational plots at various resolutions, r/r_0 ,

$$(\log(r/r_0), \log \langle (\varepsilon_{r_0})^q \rangle - \log \langle (\varepsilon_r)^q \rangle), \quad (11)$$

where the expectation is also taken across all profiles.

The scalings for several moments are shown in Fig. 3. Gathering various slope values, the observational curve of $(q, K(q))$ in the range of $0 \leq q \leq 2$ is indicated in Fig. 4 in cyan. Considering the error for $K(q)$ at each q , the theoretical curve for the multifractal model (Eq. (6)) is fitted to the data. The best fit curve (black curve in Fig. 4) has a multifractal index of $\alpha = 1.74 \pm 0.01$, and the codimension of the mean is $C_1 = 0.393 \pm 0.001$. These values are largely consistent with previous results for atmospheric dissipation fields ($\alpha = 1.35 \pm 0.07$, $C_1 = 0.3 \pm 0.05$ for the horizontal shear of a velocity field³⁰; $\alpha = 1.85 \pm 0.05$, $C_1 = 0.59 \pm 0.05$ for vertical kinetic energy flux³¹).

Figure 5 shows the theoretical curve of extremes for the multifractal model (Eq. (7)).

$$c(\gamma) = C_1 \left(\frac{\gamma}{C_1 \alpha'} + \frac{1}{\alpha} \right)^{\alpha'}, \quad \frac{1}{\alpha} + \frac{1}{\alpha'} = 1 \quad (12)$$

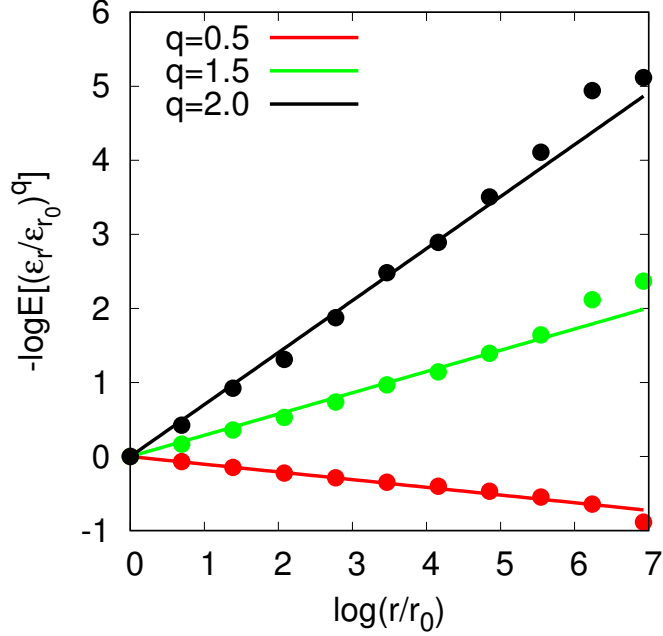


Figure 3. Scale dependency of the moments, $(\log(r/r_0), -\log\langle(\varepsilon_r/\varepsilon_{r_0})^q\rangle)$, where r_0 is the width of observational bin. The moment scaling exponents are derived as $K(0.5) = -0.104 \pm 0.006$, $K(1.5) = 0.287 \pm 0.023$, $K(2.0) = 0.702 \pm 0.036$.

in black and the observational curve,

$$c_{\text{obs}}(\gamma) = -\log_{\lambda} [g(\gamma)Pr(\varepsilon_{r_0}/\varepsilon_L > \lambda^{\gamma})], \quad \lambda = L/r_0, \quad (13)$$

in cyan, where $\lambda = 2^8$ is used, which is a typical scale ratio in the data. Note that the correction term,

$$g(\gamma) = \sqrt{2\pi\alpha c(\gamma) \log \lambda}, \quad (14)$$

serves to compensate for the prefactor in asymptotic complementary cumulative distribution function, $g(\gamma)^{-1}e^{-c(\gamma)}$ [32, Eq. 1.2.11]. The two curves (12) and (13) appear to be in good agreement. Moreover, as our data have sampling dimension $D_s = \log_{\lambda} N_s \simeq \log 400 / \log(2^8) = 1.08$, the upper bound for q is calculated to be $q_s = 2.60$ (the slope of the navy line in Fig. 5), which justifies the range we set ($0 \leq q \leq 2$).

To demonstrate the appropriateness of the universal multifractal model, the histogram for the logarithm of bin values in observational data is shown in Fig. 6 and compared with samples from multiplicative cascade models, which are detailed in sec. 3.1. Each bin value, ε_{r_0} , is normalized by the arithmetic mean, ε_L , along the profile it belongs to. The histogram for the logarithm of bin data, $\log_{10}(\varepsilon_{r_0}/\varepsilon_L)$, appears to be in good agreement with the histogram of samples generated by the 8-step cascade model with stable Lévy generators (black; $\alpha = 1.74$, $C_1 = 0.393$) and in poor agreement with the histogram generated by the multifractal model with Gaussian generators (red; $\alpha = 2$, $C_1 = 0.397$).

Moreover, in the same manner as the correlation in Yaglom's cascade, it is shown that the observational profiles have a power-law autocorrelation,

$$\langle \varepsilon(z)\varepsilon(z+\ell) \rangle \propto \ell^{-K(2)} = \ell^{-0.702}, \quad (15)$$

where z is depth. This also explains the discontinuous characteristics observed in the profiles (see Fig. 2(a)).

3 Estimations based on the cascade model

3.1 Multiplicative cascade simulation

To examine the relationship between various statistical quantities derived from observational profiles, we construct a simulation model for the multiplicative cascade by following the procedure described in Schmitt (2003)³³, as shown in Fig. 7. Each

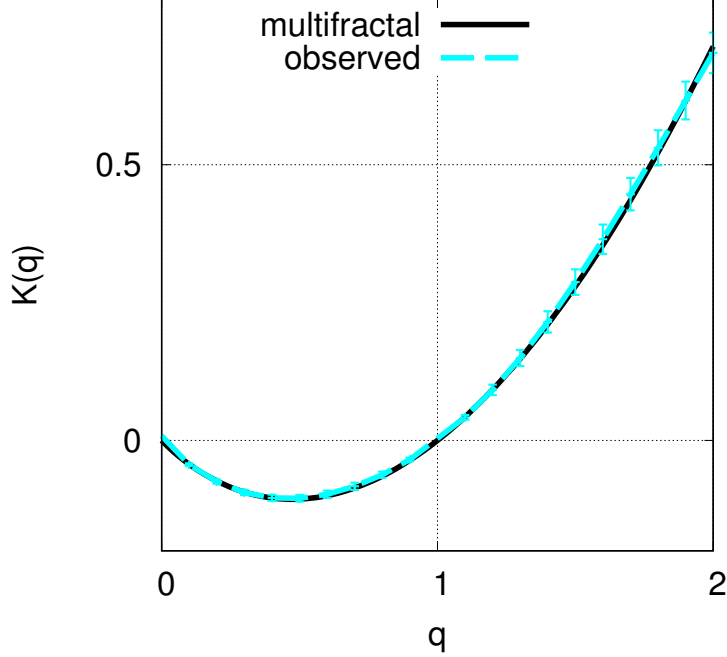


Figure 4. Moment scaling exponent $K(q)$ for observational data (cyan), and the best-fitting multifractal model (black). Each error bar in cyan shows the standard deviation for each $K(q)$.

building block, Γ_{ik} , is a generator that obeys a left-skewed stable distribution, $S_\alpha(\sigma h^{1/\alpha}, -1, -\widehat{\sigma}_\alpha^\alpha h)$, with $h \equiv \log 2$, $\widehat{\sigma}_\alpha^\alpha \equiv \sigma^\alpha / \cos(\frac{\pi}{2}(2-\alpha)) = C_1/(\alpha-1)$ ³².

Consider a fixed horizontal position \vec{x} . Let $\bar{\epsilon} = \exp(\bar{\gamma})$ be the energy input rate from an external force at \vec{x} , the number of steps be $n = \log_2 \frac{L}{r}$, $0 \leq i \leq n$ be scale index, and $1 \leq j \leq 2^n$ be spatial index. The cascade simulation is performed for variable $X_{i,j}$ as follows.

1. For each spatial index $j = 1, 2, \dots, 2^n$, set $X_{0,j} = \bar{\gamma}$.
2. For each scale index $i = 1, \dots, n$, repeat the following steps:
 - For each spatial block $k = 1, 2, \dots, 2^i$, perform the following steps:
 - (a) Generate a random variable, ξ_{ik} , which obeys $S_\alpha(1, -1, 0)$ ³⁴.
 - (b) For each spatial index $j = (k-1) \cdot 2^{n-i} + 1, \dots, k \cdot 2^{n-i}$, downscale X by

$$X_{i,j} = X_{i-1,j} + \Gamma_{i,k}, \quad \Gamma_{i,k} \stackrel{\text{def}}{=} -\widehat{\sigma}_\alpha^\alpha h + \sigma h^{\frac{1}{\alpha}} \xi_{ik}. \quad (16)$$

- For each spatial index $j = 1, 2, \dots, 2^n$, set $\gamma_j = X_{n,j}$.

The output, γ_j , represents the logarithm of energy dissipation rate at the horizontal position, \vec{x} , and the vertical position, $z_j \in [(j-1)r_n, jr_n]$ at resolution $r_n = L/2^n$. By use of the Gauss symbol, the cascade process can be more compactly represented as

$$\gamma_j = \bar{\gamma} + \sum_{i=1}^n \Gamma_{i, [(j-1)/2^{n-i}]+1}, \quad j = 1, 2, \dots, 2^n, \quad (17)$$

An important implication in this formulation is that the arithmetic average of the vertical data points is not necessarily equal to the the energy input rate because the cascade process has a fluctuating nature. In other words, a realization of the vertical average, $2^{-n} \sum_{j=1}^{2^n} \exp(\gamma_j)$, is not always equal to $\bar{\gamma}$, whereas expectation $\mathbb{E} \left[2^{-n} \sum_{j=1}^{2^n} \exp(\gamma_j) \right]$ is $\bar{\gamma}$. Below, we focus mainly on the relationship between the arithmetic average over a profile and the energy input rate. We perform statistical estimations from one to the other of these quantities based on the cascade model.

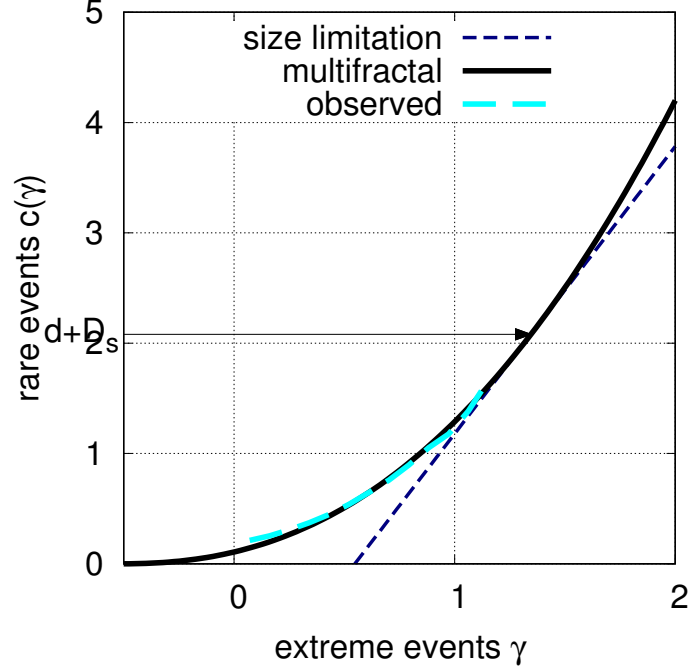


Figure 5. Codimension $c(\gamma)$ of singularities γ for multifractal model (black). The corresponding curve for observation is shown for reference (cyan). Sampling dimension D_s , and the limitation for the moment exponent (the slope of the navy line) are also shown.

3.2 Estimation of the energy input rate

In this section, we discuss how to estimate the energy input rate, $\bar{\epsilon}$, by utilizing the information obtained from an observational profile. Even though it is primarily indicated by the arithmetic average of vertical data values, as shown in the previous subsection, there still is a requirement for obtaining uncertainty information. For this purpose, we will estimate the confidence interval, the interval within which “the population mean”, $\bar{\gamma}$, is expected to lie with a defined probability. It can be evaluated by using the joint probability density of several sample statistics, obtained from Monte Carlo simulation of the cascade model. The notation used in this section is summarized in table 1.

3.2.1 Estimation technique

We assume that each γ_j 's are generated by an n -step cascade model as in Eq. (17). What we want to estimate here is the energy input rate $\bar{\gamma}$, which corresponds to a population mean, using the information from observed data $\{\gamma_j | j = 1, 2, \dots, 2^n\}$. In this regard, we first take note of the following expressions based on Eq. (17):

$$\hat{\gamma} = \bar{\gamma} + \log \left\{ 2^{-n} \sum_{j=1}^{2^n} \exp \left(\sum_{i=1}^n \Gamma_{i, [(j-1)/2^{n-i} + 1]} \right) \right\}, \quad (18)$$

$$\tilde{\gamma} = \bar{\gamma} + 2^{-n} \sum_{j=1}^{2^n} \sum_{i=1}^n \Gamma_{i, [(j-1)/2^{n-i} + 1]}, \quad (19)$$

$$\gamma^\sharp = \bar{\gamma} + \frac{1}{2} \log \left\{ 2^{-n} \sum_{j=1}^{2^n} \exp \left(2 \sum_{i=1}^n \Gamma_{i, [(j-1)/2^{n-i} + 1]} \right) \right\}, \quad (20)$$

where we find the term $\bar{\gamma}$ is factored out. Therefore, $\bar{\gamma} - \hat{\gamma}$, $\hat{\gamma} - \tilde{\gamma}$, and $\hat{\gamma} - \gamma^\sharp$ are independent of $\bar{\gamma}$, and also dimensionless.

The structure of cascade model implies that the appearance probability of $\hat{\gamma}$ given $\bar{\gamma}$ is determined only by their difference: $P(\hat{\gamma} | \bar{\gamma}) = q_1(\bar{\gamma} - \hat{\gamma})$. Furthermore, by assuming that we have no prior information about $\bar{\gamma}$, Bayes' theorem applies to invert it into the posterior probability for $\bar{\gamma}$ as follows.

$$P(\bar{\gamma} | \hat{\gamma}) = \frac{P(\hat{\gamma} | \bar{\gamma}) P(\bar{\gamma})}{\int P(\hat{\gamma} | \bar{\gamma}) P(\bar{\gamma}) d\bar{\gamma}} = q_1(\bar{\gamma} - \hat{\gamma}). \quad (21)$$

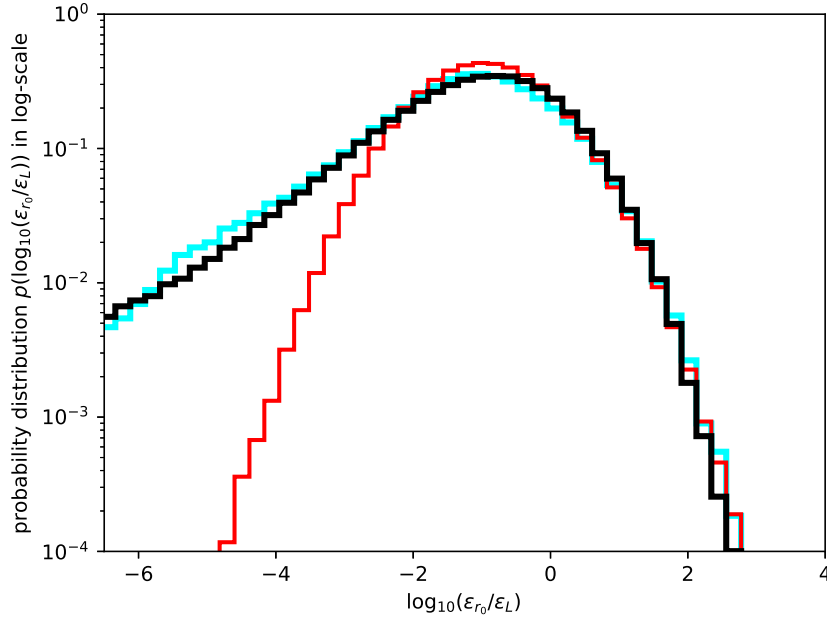


Figure 6. Distribution of the logarithm of observational data normalized for each profile (cyan) and comparison with the statistics of samples generated from multiplicative cascade with Gaussian/stable Lévy generators (red/black).

In order to take also into account the information from $\tilde{\gamma}$ and γ^\sharp , we use joint probability distribution $q_3(\bar{\gamma} - \hat{\gamma}, \hat{\gamma} - \tilde{\gamma}, \hat{\gamma} - \gamma^\sharp)$ to derive a conditional probability distribution:

$$q_3(\bar{\gamma} - \hat{\gamma} | \hat{\gamma} - \tilde{\gamma}, \hat{\gamma} - \gamma^\sharp) = \frac{q_3(\bar{\gamma} - \hat{\gamma}, \hat{\gamma} - \tilde{\gamma}, \hat{\gamma} - \gamma^\sharp)}{\int q_3(\bar{\gamma} - \hat{\gamma}, \hat{\gamma} - \tilde{\gamma}, \hat{\gamma} - \gamma^\sharp) d\bar{\gamma}}. \quad (22)$$

The similar procedure as in Eq. (21) applies to obtain the posterior probability:

$$P(\bar{\gamma} | \hat{\gamma}, \hat{\gamma} - \tilde{\gamma} = u, \hat{\gamma} - \gamma^\sharp = v) = q_3(\bar{\gamma} - \hat{\gamma} | u, v), \quad (23)$$

under the constraint of $\hat{\gamma} - \tilde{\gamma} = u, \hat{\gamma} - \gamma^\sharp = v$.

On the basis of the above formulation, we perform an identical twin experiment in the following procedure.

1. Perform a Monte Carlo experiment to obtain $q_3(\bar{\gamma} - \hat{\gamma}, \hat{\gamma} - \tilde{\gamma}, \hat{\gamma} - \gamma^\sharp)$.
 - (a) Set the energy input rate to $\bar{\gamma} = 0$.
 - (b) Create many random samples of profile using the cascade model according to procedure in sec. 3.1.
 - (c) Add up the frequency of occurrence to derive the joint probability distribution $q_3(\bar{\gamma} - \hat{\gamma}, \hat{\gamma} - \tilde{\gamma}, \hat{\gamma} - \gamma^\sharp)$.
2. Set the energy input rate $\bar{\gamma}$ to a random number.
3. Create a random sample of profile using the cascade model according to procedure in sec. 3.1.
4. Calculate the parameters $\hat{\gamma}, \hat{\gamma} - \tilde{\gamma}, \hat{\gamma} - \gamma^\sharp$ for the profile.
5. Compute the conditional probability distribution $P(\bar{\gamma} | \hat{\gamma}, \hat{\gamma} - \tilde{\gamma}, \hat{\gamma} - \gamma^\sharp)$.
6. Calculate the median and 95% confidence interval for estimated $\bar{\gamma}$.
7. Compare the estimate of $\bar{\gamma}$ with the true value of $\bar{\gamma}$.

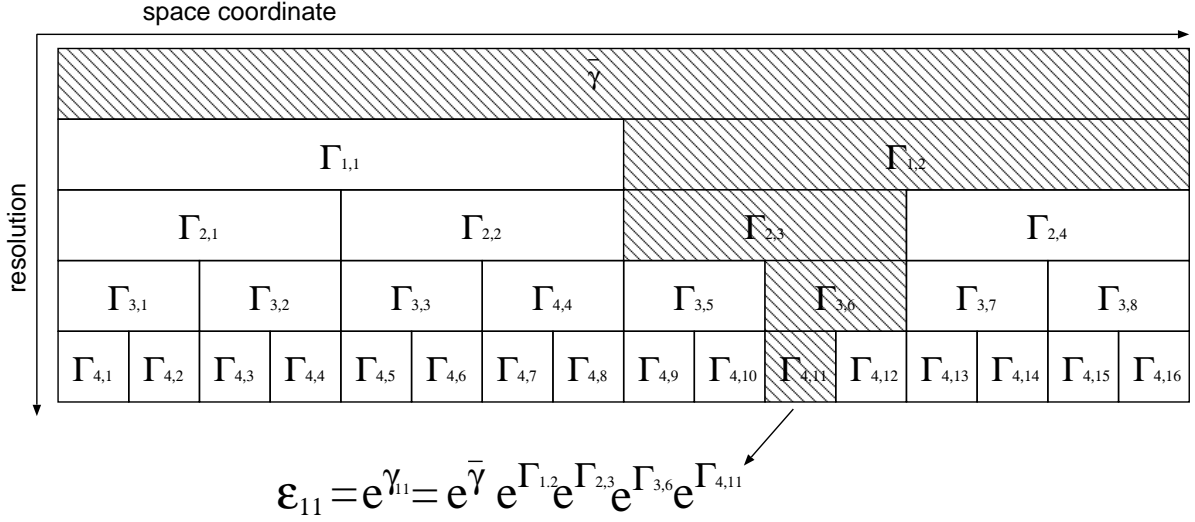


Figure 7. Schematic of the multiplicative cascade model. The energy dissipation rate at z_{11} at resolution $r_4 = L/2^4$ is considered as an example.

The same procedure applies to real data experiment, except that $\bar{\gamma}$ in 2 is unknown, as follows.

1. Pick an observed profile, and calculate the parameters $\hat{\gamma}, \hat{\gamma} - \tilde{\gamma}, \hat{\gamma} - \gamma^\sharp$ for the profile.
2. Compute the conditional probability distribution $P(\bar{\gamma} | \hat{\gamma}, \hat{\gamma} - \tilde{\gamma}, \hat{\gamma} - \gamma^\sharp)$, using the joint probability distribution $q_3(\bar{\gamma} - \hat{\gamma}, \hat{\gamma} - \tilde{\gamma}, \hat{\gamma} - \gamma^\sharp)$ obtained from the Monte Carlo experiment.
3. Calculate the median and 95% confidence interval for estimated $\bar{\gamma}$.

3.2.2 Simulation of joint probability distribution

We perform a Monte Carlo experiment with simulations of 1.024×10^{10} particles using the 8-step cascade model. For each particle, we generate random numbers $\{\gamma_j | j = 1, 2, \dots, 2^N\}$ according to the procedure given in sec. 3.1, and add up for all the particles into the joint probability distribution $q_3(\bar{\gamma} - \hat{\gamma}, \hat{\gamma} - \tilde{\gamma}, \hat{\gamma} - \gamma^\sharp)$ (Fig. 8).

Examples for conditional probability distribution $q_3(\bar{\gamma} - \hat{\gamma} | u, v)$ are shown in Fig. 9. The conditional expectation for $\bar{\gamma}$ is not necessarily defined as a finite value because the posterior distribution of $\bar{\gamma}$ is neither Gaussian nor left-skewed stable. On the other hand, because the median and the percentiles, and thus the 95% confidence interval, for the distribution are always defined, we use them as the indices for estimation.

3.2.3 Identical twin experiment

The result of identical twin experiment using $q_3(\bar{\gamma} - \hat{\gamma} | \hat{\gamma} - \tilde{\gamma}, \hat{\gamma} - \gamma^\sharp)$ is shown in Fig. 10a. In 28525 trials out of 30000 (about 95%), the true value of $\bar{\gamma}$ lies within the confidence interval, which ensures the validity of the estimation method. We also performed a reference experiment using $q_1(\bar{\gamma} - \hat{\gamma})$ (Fig. 10b), where the confidence interval and median shows a common positional relation to the arithmetic mean. Comparing the case with q_3 to the one with q_1 , the root mean square of confidence interval are 3.4 and 3.6 respectively, and 84% of trials in the former have narrower confidence interval. This indicates the superiority of using information from $\tilde{\gamma}$ and γ^\sharp .

3.2.4 Real data experiment

By applying the same procedure to the real observational profiles of energy dissipation rate, each of which is represented by $\hat{\gamma}, \hat{\gamma} - \tilde{\gamma}$, and $\hat{\gamma} - \gamma^\sharp$, we derive the confidence interval of $\bar{\gamma}$ for the profile at each horizontal location. Estimated confidence intervals for real data are shown in Fig. 11b. Figure 12 shows the estimate for confidence intervals on the sections along 47°N and 137°E. Along 47°N, the median of $\bar{\gamma}$ rarely exceed $10^{-9} \text{m}^2 \text{s}^{-3}$, except around 170°E, 180°E, or 50°W. The peak of arithmetic mean at 170°E is about 4 times larger than the median estimate, which could lead us to an overestimation.

Along 137°E, the median shows several significant peaks over $10^{-8} \text{m}^2 \text{s}^{-3}$ at around 2°N, 16°N, and 27°N. We could have underestimated the peaks at around 2°N and 27°N, but overestimated the one at around 16°N, if we only used the arithmetic mean.

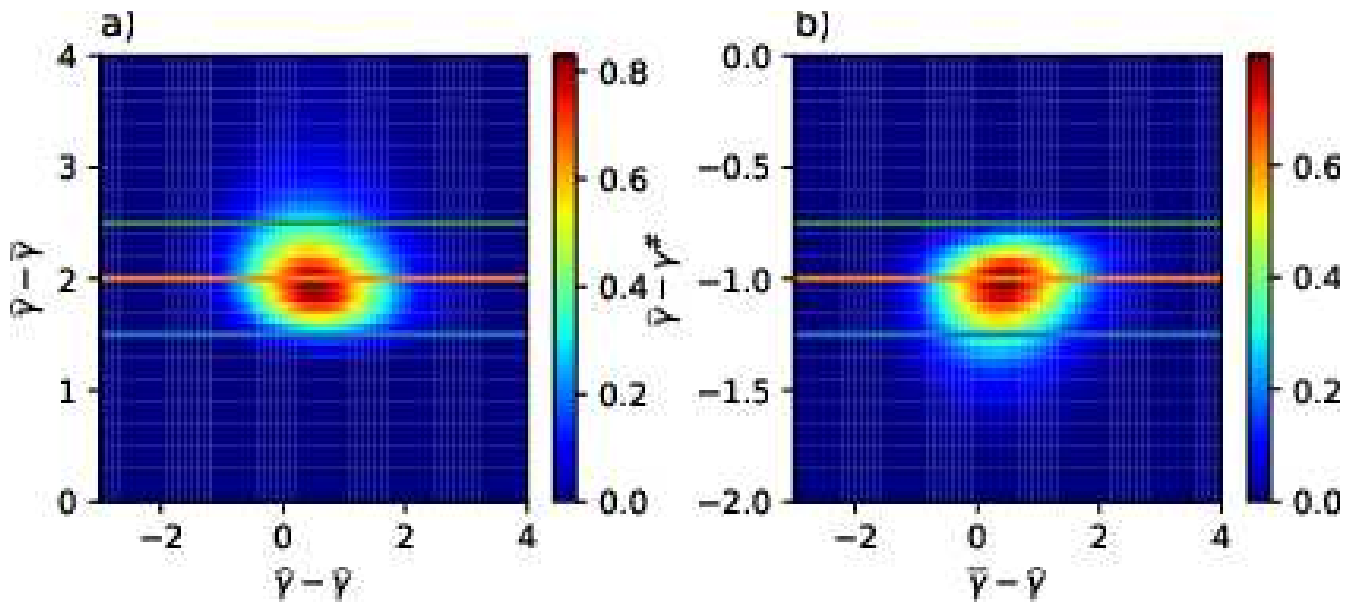


Figure 8. Examples of cross section cut of joint probability distribution $q_3(\bar{\gamma} - \hat{\gamma}, \hat{\gamma} - \tilde{\gamma}, \hat{\gamma} - \gamma^\#)$. a) section cut $q_3(\bar{\gamma} - \hat{\gamma}, \hat{\gamma} - \tilde{\gamma}, -1)$ with section lines $\hat{\gamma} - \tilde{\gamma} = 1.5, 2, 2.5$, and b) section cut $q_3(\bar{\gamma} - \hat{\gamma}, 2, \hat{\gamma} - \gamma^\#)$ with section lines $\hat{\gamma} - \gamma^\# = -1.25, -1, -0.75$.

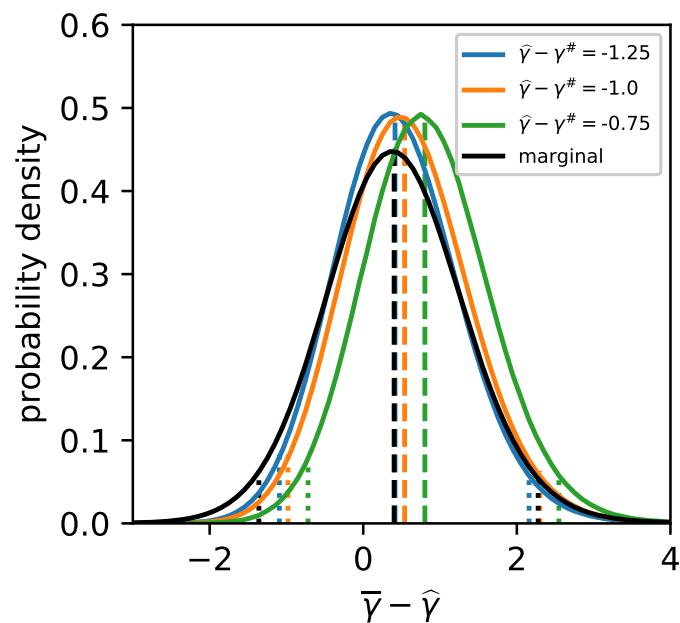


Figure 9. Examples of conditional probability distribution $q_3(\cdot | u, v)$ (colored) and marginal probability distribution $q_1(\cdot)$ (black), along with median (broken lines) and 95% confidence intervals (dotted lines). Conditional probabilities are for $u = 2; v = -1.25, -1, -0.75$.

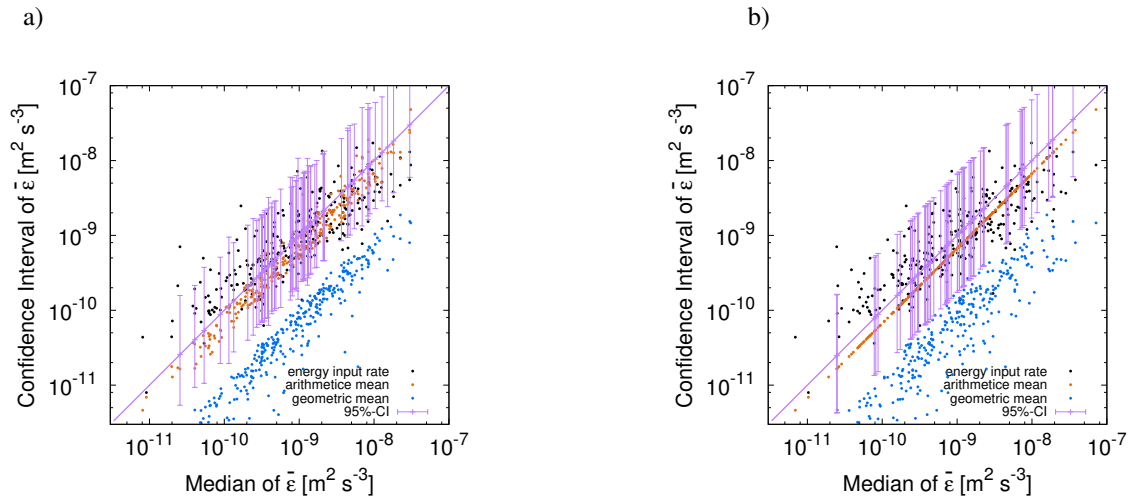


Figure 10. Result of identical twin experiments. Median (horizontal axis) versus confidence interval (vertical axis). a) result using conditional probability distribution $q_3(\cdot|u, v)$, and b) result using marginal probability distribution $q_1(\cdot)$. For a given values of median in horizontal axis, the points in vertical axis indicate the values of confidence interval (purple), arithmetic mean (orange), geometric mean (blue), and the energy input rate (black). For readability, 500 points and 100 intervals are drawn out of 50000 trials.

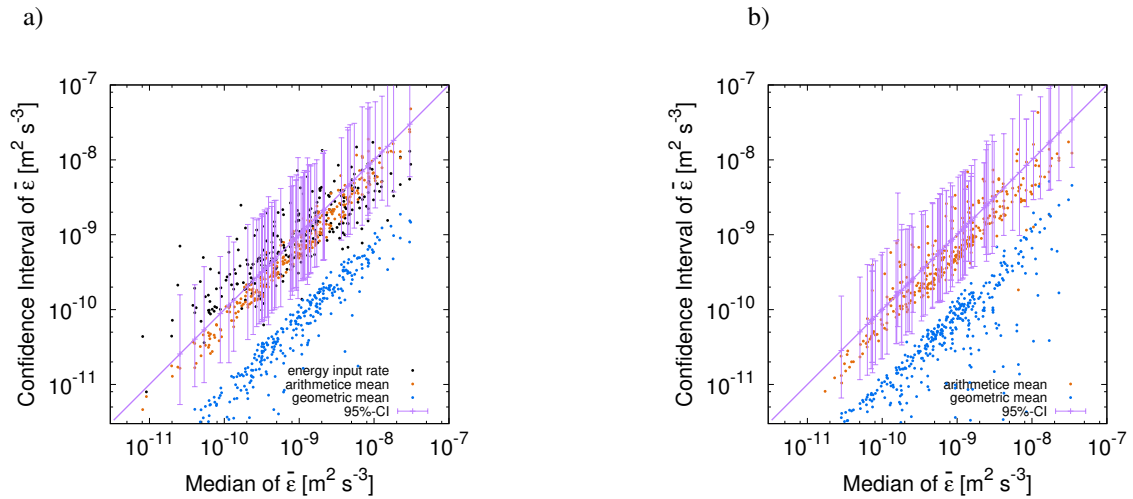


Figure 11. Result of real data experiment. Median (horizontal axis) versus confidence interval (vertical axis). a) result of identical twin experiment, and b) result of real data experiment. For a given values of median in horizontal axis, the points in vertical axis indicate the values of confidence interval (purple), arithmetic mean (orange), geometric mean (blue), and the energy input rate (black).

Table 1. Notation for the estimation study

Name	Notation	Definition
Step number of cascade	n	
Index for vertical position	j	$1, 2, 3, \dots, 2^n$
Energy dissipation rate	ε_j	
Logarithm of energy dissipation rate	γ_j	$\log \varepsilon_j$
Energy input rate	$\bar{\varepsilon}$	
Logarithm of energy input rate	$\bar{\gamma}$	$\log \bar{\varepsilon}$
Stable Lévy generators	Γ_{ik}	$\sim S_\alpha(\sigma h^{1/\alpha}, -1, -\widehat{\sigma}_\alpha^\alpha h)$
Width of Lévy generator	$\sigma h^{1/\alpha}$	
Shift of Lévy generator	$-\widehat{\sigma}_\alpha^\alpha h$	$-\frac{\sigma^\alpha}{\cos(\frac{\pi}{2}(2-\alpha))}h = -\frac{C_1}{\alpha-1}h$
Multifractal index	α	
Codimension of the mean	C_1	
Step size of cascade	h	$\log 2$
Logarithm of arithmetic mean	$\widehat{\gamma}$	$\log \left(2^{-n} \sum_{j=1}^{2^n} e^{\gamma_j} \right)$
Logarithm of geometric mean	$\widetilde{\gamma}$	$2^{-n} \sum_{j=1}^{2^n} \gamma_j$
Logarithm of quadratic mean	γ^\sharp	$\frac{1}{2} \log \left(2^{-n} \sum_{j=1}^{2^n} e^{2\gamma_j} \right)$
Marginal probability distribution	q_1	Probability distribution of $\bar{\gamma} - \widehat{\gamma}$
Joint probability distribution	q_3	Probability distribution of $(\bar{\gamma} - \widehat{\gamma}, \widehat{\gamma} - \widetilde{\gamma}, \widetilde{\gamma} - \gamma^\sharp)$

For the analysis of observations on the section along 165°E, we should take care of the effect of repeated observation. In fact, the observations were performed twice at some horizontal locations there. For such cases, we simply assume that two independent realizations of a common $\bar{\gamma}$ are observed. In this regard, the inversion formula in Eq. (21) is modified as follows.

$$P(\bar{\gamma}|\widehat{\gamma}_1, \widehat{\gamma}_2) = \frac{P(\widehat{\gamma}_1, \widehat{\gamma}_2|\bar{\gamma})P(\bar{\gamma})}{\int P(\widehat{\gamma}_1, \widehat{\gamma}_2|\bar{\gamma})P(\bar{\gamma})d\bar{\gamma}} = \frac{P(\widehat{\gamma}_1|\bar{\gamma})P(\widehat{\gamma}_2|\bar{\gamma})P(\bar{\gamma})}{\int P(\widehat{\gamma}_1|\bar{\gamma})P(\widehat{\gamma}_2|\bar{\gamma})P(\bar{\gamma})d\bar{\gamma}} = \frac{q_1(\bar{\gamma} - \widehat{\gamma}_1)q_1(\bar{\gamma} - \widehat{\gamma}_2)}{\int q_1(\bar{\gamma} - \widehat{\gamma}_1)q_1(\bar{\gamma} - \widehat{\gamma}_2)d\bar{\gamma}}, \quad (24)$$

where two observations are distinguished by subscript 1, 2. This distribution is nothing but the normalized product of the two distributions. When considering $\widetilde{\gamma}$ and γ^\sharp , the same procedure as in Eq. (24) applies to the conditional distribution:

$$\begin{aligned} P(\bar{\gamma}|\widehat{\gamma}_1, \widehat{\gamma}_2, \widehat{\gamma}_1 - \widetilde{\gamma}_1 = u_1, \widehat{\gamma}_1 - \gamma^\sharp_1 = v_1, \widehat{\gamma}_2 - \widetilde{\gamma}_2 = u_2, \widehat{\gamma}_2 - \gamma^\sharp_2 = v_2) \\ = \frac{q_3(\bar{\gamma} - \widehat{\gamma}_1|u_1, v_1)q_3(\bar{\gamma} - \widehat{\gamma}_2|u_2, v_2)}{\int q_3(\bar{\gamma} - \widehat{\gamma}_1|u_1, v_1)q_3(\bar{\gamma} - \widehat{\gamma}_2|u_2, v_2)d\bar{\gamma}}. \end{aligned} \quad (25)$$

Figure 13b shows the estimation of confidence interval along 165°E, by taking into account the effect of repeated observation. For comparison, the result without considering the repeated observation is shown in Fig. 13a, where we assume that each observation is for different $\bar{\gamma}$. We can see that the confidence intervals become narrower when considering the effect of repeated observation. Also, along 165°E, the median shows a broad and significant peak over $10^{-8}\text{m}^2\text{s}^{-3}$ at around 30°N.

Discussion

We have analyzed the observed data obtained from oceanic turbulence and shown that the vertical sequences of energy dissipation rates have an intermittent structure that obeys a scaling law. Furthermore, we have proposed a method of estimating the energy input rate given observations by utilizing that property.

1. For scaling in the observed profiles, the statistical property of our data is consistent with the universal multifractal model, which has a moment scaling exponent of $K(q) = \frac{C_1}{\alpha-1}(q^\alpha - q)$ with a multifractal index $\alpha = 1.74$ and the codimension of the mean $C_1 = 0.393$. This result elucidates the universality inherent in the oceanic turbulence data.
2. The energy input rate and its uncertainty can be estimated by an inference using the result of Monte Carlo simulation of the cascade model. This method utilizes the observed values of arithmetic mean, geometric mean, and quadratic mean over a profile. The estimate provides an additional information about uncertainty of energy input rate, which exhibits an increased accuracy than the one obtained from the arithmetic mean alone.

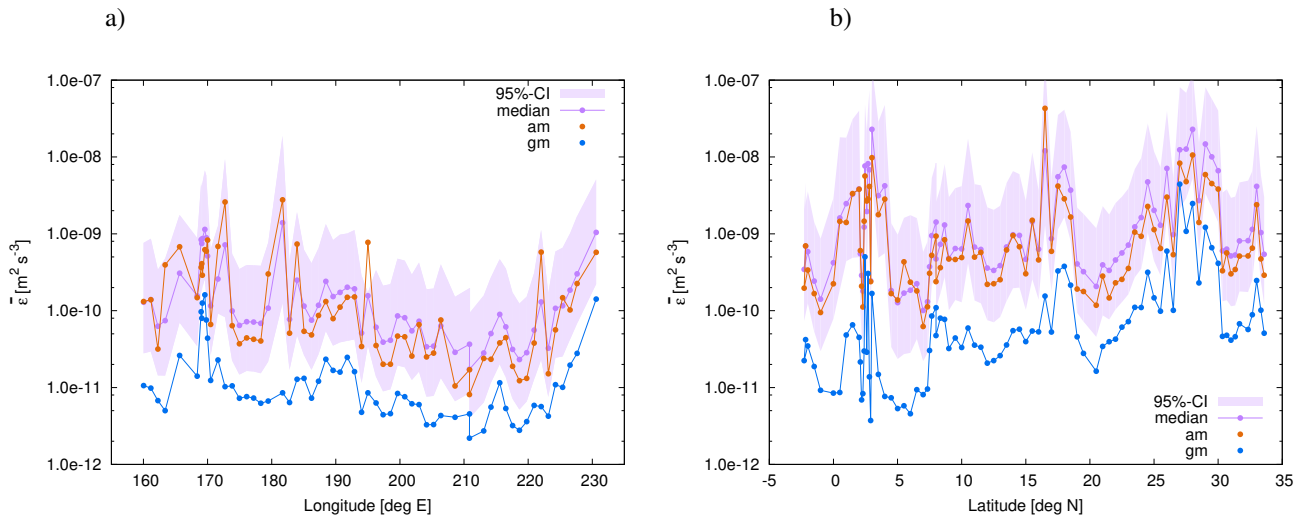


Figure 12. Geographical distribution of confidence intervals. 47°N (a) and 137°E (b). Horizontal axis shows the location, and the values of median (purple dots) and confidence interval (purple shade), arithmetic mean (orange)m and geometric mean (blue) are on the vertical axis.

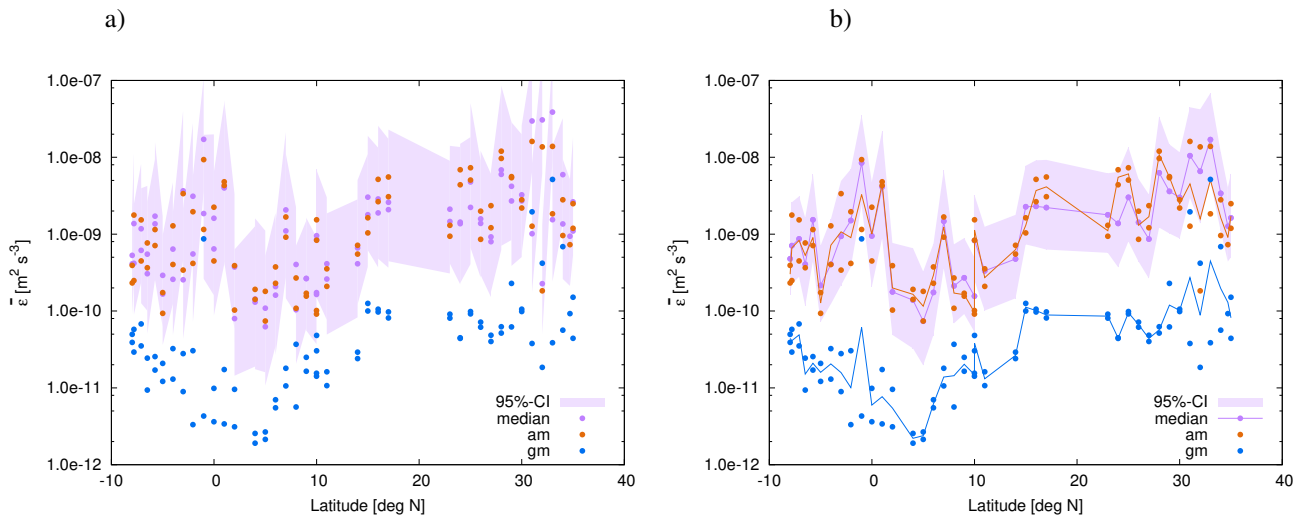


Figure 13. Geographical distribution of confidence intervals. 165°E. The effect of repeated observation is considered in a), but not in b). Horizontal axis shows the location, and the values of median (purple dots) and confidence interval (purple shade), arithmetic mean (orange)m and geometric mean (blue) are on the vertical axis.

3. Theoretically, this technique can easily be extended by utilizing more statistics over a profile than arithmetic mean, geometric mean, and quadratic mean. Note however that such extension may easily provoke the curse of dimensionality, and thus can become impractical.
4. Thus, we have found an answer to the question: “how can one estimate energy input rate from the vertical profile data of the energy dissipation rate?” By analyzing the intermittency in the observed data, we can construct a multiplicative cascade model based on the universal multifractal formalism, which can reproduce the statistics of the data. Then, the energy input rate given observed data is estimated by inverting the probability distribution obtained from Monte Carlo simulations of the cascade model.
5. Even though we have used a discrete cascade model for simplicity and computational viability, we can extend it to a continuous cascade³⁵, which may improve the estimation accuracy at the cost of computational burden.

References

1. Gregg, M., Cox, C. & Hacker, P. Vertical Microstructure Measurements in the Central North Pacific. *J. Phys. Oceanogr.* **3**, 458–469 (1973).
2. Munk, W. & Wunsch, C. Abyssal recipes II: Energetics of tidal and wind mixing. *Deep. Sea Res. Part I: Oceanogr. Res. Pap.* **45**, 1977–2010 (1998).
3. Waterhouse, A. F. *et al.* Global patterns of diapycnal mixing from measurements of the turbulent dissipation rate. *J. Phys. Oceanogr.* **44**, 1854–1872, DOI: [10.1175/JPO-D-13-0104.1](https://doi.org/10.1175/JPO-D-13-0104.1) (2014). <https://doi.org/10.1175/JPO-D-13-0104.1>.
4. Waterhouse, A. & McKinnon, J. Datasets obtained from ocean microstructure profilers (2014).
5. Pope, S. B. *Turbulent flows* (Cambridge university press, 2000).
6. Richardson, L. F. *Weather Prediction by Numerical Process* (Cambridge University, Cambridge, 1922).
7. Kolmogorov, A. N. The local structure of turbulence in incompressible viscous fluid for very large Reynolds numbers. *Cr Acad. Sci. URSS* **30**, 301–305 (1941).
8. Landau, L. D. & Lifshitz, E. M. Fluid mechanics. *Fluid Mech. Second. Ed. 1987. Pergamon, Oxf.* (1987).
9. Kolmogorov, A. N. A refinement of previous hypotheses concerning the local structure of turbulence in a viscous incompressible fluid at high Reynolds number. *J. Fluid Mech.* **13**, 82–85 (1962).
10. Gurvich, A. & Zubkovskii, S. On experimental estimate of the fluctuations of turbulent energy dissipation. *Izv. Akad. Nauk SSSR, Ser. Geofiz* **12**, 1856 (1963).
11. Pond, S. & Stewart, R. W. Measurement of statistical characteristics of small-scale turbulence. *Izv. Akad. Nauk SSSR, Ser. Geofiz* **1**, 914 (1965).
12. Yaglom, A. M. The influence of fluctuations in energy dissipation on the shape of turbulent characteristics in the inertial interval. *Sov. Phys. Dokl.* **11** (1966).
13. Monin, A. S. & Yaglom, A. M. *Statistical fluid mechanics, volume II: mechanics of turbulence*, vol. 2, chap. 8 (Courier Corporation, 2013).
14. Frisch, U., Sulem, P.-L. & Nelkin, M. A simple dynamical model of intermittent fully developed turbulence. *J. Fluid Mech.* **87**, 719–736 (1978).
15. Benzi, R., Paladin, G., Parisi, G. & Vulpiani, A. On the multifractal nature of fully developed turbulence and chaotic systems. *J. Phys. A: Math. Gen.* **17**, 3521 (1984).
16. Schertzer, D. & Lovejoy, S. Elliptical turbulence in the atmosphere. In *Symposium on Turbulent Shear Flows, 4 th, Karlsruhe, West Germany*, 11 (1984).
17. Meneveau, C. & Sreenivasan, K. Simple multifractal cascade model for fully developed turbulence. *Phys. review letters* **59**, 1424 (1987).
18. Schertzer, D. & Lovejoy, S. Physical modelling and analysis of rain and clouds by anisotropic scaling and multiplicative processes. *J. Geophys. Res.* **92**, 9693–9714 (1987).
19. She, Z.-S. & Leveque, E. Universal scaling laws in fully developed turbulence. *Phys. review letters* **72**, 336 (1994).
20. Schmitt, F. G. & Huang, Y. *Homogeneous turbulence and intermittency*, 12–40 (Cambridge University Press, 2016).

21. Goto, Y., Yasuda, I. & Nagasawa, M. Comparison of Turbulence Intensity from CTD-Attached and Free-Fall Microstructure Profilers. *J. Atmospheric Ocean. Technol.* **35**, 147–162, DOI: [10.1175/JTECH-D-17-0069.1](https://doi.org/10.1175/JTECH-D-17-0069.1) (2018).
22. Batchelor, G. K. Small-scale variation of convected quantities like temperature in turbulent fluid Part 1. General discussion and the case of small conductivity. *J. Fluid Mech.* **5**, 113–133, DOI: [10.1017/S002211205900009X](https://doi.org/10.1017/S002211205900009X) (1959).
23. Ruddick, B., Anis, A. & Thompson, K. Maximum Likelihood Spectral Fitting: The Batchelor Spectrum. *J. Atmospheric Ocean. Technol.* **17**, 1541–1555 (2000).
24. Kraichnan, R. H. Small-scale structure of a scalar field convected by turbulence. *The Phys. Fluids* **11**, 945–953 (1968).
25. Goto, Y., Yasuda, I. & Nagasawa, M. Turbulence Estimation Using Fast-Response Thermistors Attached to a Free-Fall Vertical Microstructure Profiler. *J. Atmospheric Ocean. Technol.* **33**, 2065–2078, DOI: [10.1175/JTECH-D-15-0220.1](https://doi.org/10.1175/JTECH-D-15-0220.1) (2016).
26. Lovejoy, S. & Schertzer, D. *The Weather and Climate: Emergent Laws and Multifractal Cascades* (Cambridge University Press, 2013).
27. Gires, A., Tchiguirinskaia, I., Schertzer, D. & Lovejoy, S. Development and analysis of a simple model to represent the zero rainfall in a universal multifractal framework. *Nonlinear Process. Geophys.* **20**, 343–356 (2013).
28. Parisi, G. & Frish, U. *A multifractal model of intermittency*, 111–114 (Elsevier North Holland, New-York, 1985).
29. Schertzer, D. & Lovejoy, S. Universal multifractals do exist! *J. Appl. Meteorol.* **36**, 1296–1303 (1997).
30. Chigirinskaya, Y., Schertzer, D., Lovejoy, S., Lazarev, A. & Ordanovich, A. Unified multifractal atmospheric dynamics tested in the tropics: part I, horizontal scaling and self criticality. *Nonlinear Process. Geophys.* **1**, 105–114, DOI: [10.5194/npg-1-105-1994](https://doi.org/10.5194/npg-1-105-1994) (1994).
31. Lazarev, A., Schertzer, D., Lovejoy, S. & Chigirinskaya, Y. Unified multifractal atmospheric dynamics tested in the tropics: part II, vertical scaling and generalized scale invariance. *Nonlinear Process. Geophys.* **1**, 115–123, DOI: [10.5194/npg-1-115-1994](https://doi.org/10.5194/npg-1-115-1994) (1994).
32. Samorodnitsky, G. & Taqqu, M. S. *Non-Gaussian Stable Processes: Stochastic Models with Infinite Variance*. Chapman Hall, Lond. (1994).
33. Schmitt, F. G. Modeling of Turbulent Intermittency: Multifractal Stochastic Processes and Their Simulation. In Seuront, L. & Strutton, P. G. (eds.) *Handbook of scaling methods in aquatic ecology: measurement, analysis, simulation*, chap. 29, 453–468 (CRC Press, 2003).
34. Misiorek, A. & Weron, R. *Heavy-Tailed Distributions in VaR Calculations*, 1025–1059 (Springer Berlin Heidelberg, Berlin, Heidelberg, 2012).
35. Schmitt, F. & Marsan, D. Stochastic equations generating continuous multiplicative cascades. *The Eur. Phys. J. B-Condensed Matter Complex Syst.* **20**, 3–6 (2001).
36. Roget, E., Lozovatsky, I., Sanchez, X. & Figueroa, M. Microstructure measurements in natural waters: Methodology and applications. *Prog. Oceanogr.* **70**, 126–148 (2006).
37. Peterson, A. K. & Fer, I. Dissipation measurements using temperature microstructure from an underwater glider. *Methods Oceanogr.* **10**, 44–69 (2014).
38. Antonia, R. & Orlandi, P. On the Batchelor constant in decaying isotropic turbulence. *Phys. Fluids* **15**, 2084–2086 (2003).
39. Bogucki, D., Domaradzki, J. A. & Yeung, P. Direct numerical simulations of passive scalars with $Pr > 1$ advected by turbulent flow. *J. Fluid Mech.* **343**, 111–130 (1997).
40. Bogucki, D., Luo, H. & Domaradzki, J. Experimental evidence of the Kraichnan scalar spectrum at high reynolds numbers. *J. Phys. Oceanogr.* **42**, 1717–1728 (2012).
41. Sanchez, X., Roget, E., Planella, J. & Forcat, F. Small-scale spectrum of a scalar field in water: the Batchelor and Kraichnan models. *J. Phys. Oceanogr.* **41**, 2155–2167 (2011).

A Principle for the estimation of turbulent energy dissipation rate ε from fast-response thermistor measurements

ε is estimated from the spectra of temperature vertical gradient $\partial T' / \partial z$ using fast-response thermistor FP07 measurements, with a time constant of approximately 7×10^{-3} s (Fig. 14). The Fourier-transformed observed wavenumber temperature gradient spectrum (blue curve) is numerically integrated between the lowest wavenumber and the highest wavenumber at which

the spectrum amplitude is more than 1.5 times the noise spectrum (light-blue curve), which is inherent in the instrument, and thermal dissipation rate χ is obtained ($= 6\kappa_T \overline{\left(\frac{\partial T}{\partial z}\right)^2}$, κ_T is the molecular thermal diffusivity). ε is estimated by detecting wavenumber k_p at the peak of the temperature gradient spectrum to yield the Batchelor wavenumber, $k_B (= \left(\frac{\varepsilon}{\nu\kappa_T^2}\right)^{1/4} / 2\pi)^{22}$, as $k_B = \sqrt{6q_K}k_p$, at which molecular thermal diffusion begins to work. This peak is detected by fitting the theoretically derived universal temperature gradient spectrum,²⁴ $S_{\text{theoretical}}$ (red curve) with the form given in Roget (2006)³⁶, to the observed spectrum using the maximum likelihood method developed by Ruddick²³ with the parameters proposed by Peterson³⁷.

$$S_{\text{theoretical}}(k; k_B) = \frac{\chi\sqrt{q_K}}{\kappa_T k_B} y_k^2 \frac{\exp(-\sqrt{6}y_k)}{y_k},$$

where $y_k = \sqrt{q_K}k/k_B$ and q_K is the Kraichnan constant. q_K has been estimated as $q_K = 3.4 - 7.9$ (3.41 :³⁸; 5.26 ± 0.25 :^{39,40}, 7.9 ± 2.5 :⁴¹). We use a fixed value of $q_K = 5.26$, which was introduced in Bogucki^{39,40}. The Kraichnan spectrum is the modified version of the Batchelor spectrum²² considering the intermittency of strain fields. See Goto et al.(2016, 2018)^{21,25} for other detailed estimation procedures.

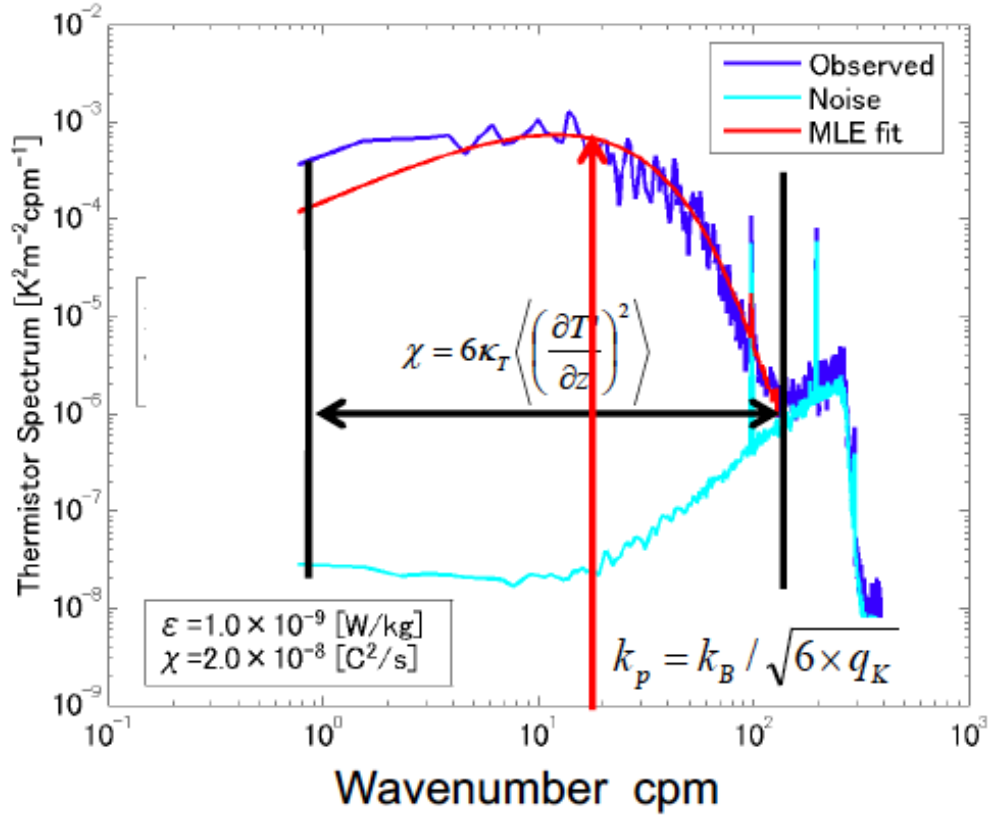


Figure 14. Example of observational wavenumber temperature gradient spectrum (blue curve), noise spectrum (light blue), and fitted theoretical spectrum (red) to detect the wavenumber at spectrum peak k_p to yield Batchelor wavenumber k_B given ε .

Acknowledgements

The helpful comments from Yutaka Yoshikawa (Kyoto University) are appreciated. This work was partially supported by Grant-in-Aid for Scientific Research on Innovative Areas (MEXT KAKENHI-JP15H05817/JP15H05819). We also thank the members of the project for their valuable discussions on the concept and method. We would like to thank Editage for English language editing. All numerical simulations were performed on the JAMSTEC Data Analyzer (DA) system.

Author contributions

SM and SO posed the main problem. IY compiled the observational data. IY, SK, SM, and SO helped formulate the hypothesis. NS proposed the method, performed the statistical analyses, and prepared the manuscript with contributions from all co-authors.